MATERIALS CHEMISTRY
FRONTIERS

RESEARCH ARTICLE

View Article Online
View Journal | View Issue

Cite this: *Mater. Chem. Front.*, 2026, **10**, 1705

Tb-doped $MA_{0.89}FA_{0.11}PbBr_3$ perovskite single crystals for gamma-ray detection

Qian Zhang,[ab] Lin Ma,*[ab] Guowei Wang,*[c] Yuhang Huang,[ab] Luyang Du,[ab] Taifeng Lin[d] and Zhengguang Yan*[ab]

Received 25th January 2026,
Accepted 12th March 2026

DOI: 10.1039/d6qm00058d

rsc.li/frontiers-materials

Rare-earth doping has emerged as a promising strategy to tailor the optoelectronic properties of metal halide perovskites, yet its potential for enhancing gamma-ray detection performance remains underexplored. The synthesis of large-sized, rare-earth doped perovskite single crystals remains challenging due to the adverse effects of dopants on crystal growth and lattice stability. Herein, we achieved 16 mm sized $MA_{0.89}FA_{0.11}PbBr_3$:Tb single crystals (Tb/Pb = 0.13–0.67%) *via* nucleation control and precursor regulation. The X-ray fluorescence mapping confirms the uniform distribution of Tb^{3+} within the crystal lattice at a low Tb/Pb ratio ($\leq$0.35%). The successful incorporation of rare earth ions and a concomitant lattice contraction profoundly enhance the charge transport characteristics. Specifically, doping with 0.13% Tb^{3+} increased the carrier mobility from 55 to 154 $cm^2\ V^{-1}\ s^{-1}$ and prolonged the carrier lifetime from 197 to 4422 ns. Consequently, the fabricated gamma-ray detector achieved a high energy resolution of 4.3% for ^{241}Am radiation (59.5 keV), a significant improvement over 15.7%. This work demonstrates rare-earth doping as an effective strategy toward high-performance perovskite radiation sensors.

1. Introduction

Halide perovskite (HP) materials have emerged as promising candidates in optoelectronics owing to their exceptional properties, including a high absorption coefficient, long carrier lifetime and diffusion length, low trap density, high carrier mobility, and tunable bandgap.[1–9] These merits make them particularly attractive for radiation detection.[10] Notably, Ni *et al.* developed a $MAPbBr_3$ single-crystal gamma-ray detector, achieving a 3.9% energy resolution for 662 keV ^{137}Cs gamma-ray spectroscopy under a 100 V bias.[11] He *et al.* realized a remarkable 1.4% energy resolution for 662 keV ^{137}Cs gamma rays using an all-inorganic $CsPbBr_3$ detector.[12] Furthermore, Zhao *et al.* and Song *et al.* have also reported high-performance gamma-ray detectors based on $FA_{0.9}Cs_{0.1}PbBr_3$ and $MAPbI_3$ single crystals, respectively, underscoring the great potential of this material family.[13,14] Recently, Dong *et al.* provided a comprehensive review on the progress and prospects of metal halide perovskites (MHPs) for next-generation optoelectronics. The advances have demonstrated that the optoelectronic characteristics of MHPs can be effectively modulated through compositional engineering, including substitution at the A, B, or X sites, which enables precise control over band gaps, carrier transport, and photoluminescence properties.[15]

Through chemical composition regulation, the semiconducting properties of HP single crystals can be further improved, with rare-earth doping serving as an effective pathway. Pan *et al.* pioneered the synthesis of $CsPbCl_3$:RE (RE = Ce^{3+}, Sm^{3+}, Eu^{3+}, Tb^{3+}, Dy^{3+}, Er^{3+}, and Yb^{3+}) nanocrystals, showcasing their potential.[16] In polycrystalline films, Zheng *et al.* and Zhang *et al.* reported that Nd^{3+} doping could enhance carrier mobility and suppress trap density in $MAPbI_3$ and α-$FAPbI_3$, leading to improved device performance.[17,18] The incorporation of RE ions often introduces lattice strain and promotes secondary nucleation, by-product formation, and the poor solubility of rare-earth reagents in organic solvents, making the growth of large, high-quality RE-doped single crystals exceedingly difficult. While a few reports exist, such as the work by Rong *et al.* on $MAPbBr_3$:Er and the work by Zi *et al.* on (Er,Yb) co-doped $MAPbI_3$ single crystals, which proved reduced trap density and increased mobility, the crystal dimensions were typically limited to the millimeter scale.[19,20] This limitation inherently restricts the large-size single crystal, leaving the full potential of RE doping in macroscopic single crystals for high-performance radiation detection largely untapped.

In this work, we overcome this critical barrier by successfully synthesizing large-sized (10–16 mm) $MA_{0.89}FA_{0.11}PbBr_3$:Tb

---

[a] *College of Materials Science and Engineering, Beijing University of Technology, Beijing 100124, China. E-mail: malin2022@bjut.edu.cn*
[b] *Beijing Key Laboratory of Microstructure and Properties of Solids, Beijing University of Technology, Beijing 100124, China*
[c] *Ordos Laboratory, Inner Mongolia 017000, People's Republic of China*
[d] *College of Chemistry and Life Science, Beijing University of Technology, Beijing, 100124, China*

(Tb/Pb = 0.13–0.67%) single crystals. Through comprehensive characterization, we prove that Tb^{3+} ions are effectively incorporated into the perovskite lattice, inducing lattice contraction and bandgap modulation. Most importantly, we demonstrate that Tb doping profoundly optimizes the charge transport properties, drastically reducing the trap density from 1.04×10^{10} cm^{-3} to 1.86×10^{9} cm^{-3} and increasing the carrier mobility from 55 cm^2 V^{-1} s^{-1} to 154 cm^2 V^{-1} s^{-1}. Furthermore, the Au/$MA_{0.89}FA_{0.11}PbBr_3$:Tb/Bi gamma-ray detectors achieve an energy resolution of 4.3% for a ^{241}Am source (59.5 keV) under a low bias of 10 V. This study not only validates rare-earth doping as a powerful strategy for property optimization but also opens new avenues for developing advanced radiation sensing materials.

2. Methods

2.1 Materials

Methylamine aqueous solution (CH_3NH_2, 40 wt% in water, Aladdin), hydrobromic acid (HBr, 40 wt% in water, Macklin), formamidine acetate (99%, Aladdin), $Pb(CH_3COO)_2{\cdot}3H_2O$ (99.5%, Fortune), $Tb(CH_3CO_2)_3{\cdot}xH_2O$ (99.99%, Aladdin), *N*,*N*-dimethylformamide (DMF, 99.5%, Aladdin) and poly(ethylene glycol) (PEG, average M_n = 1500, reagent grade, J&K Scientific) were used. All reagents were of analytical grade and used without further purification.

2.2 Synthesis of perovskite powder

$MA_{0.89}FA_{0.11}PbBr_3$ powder was synthesized by reaction among methylamine aqueous solution, formamidine acetate, lead acetate trihydrate ($Pb(Ac)_2{\cdot}3H_2O$), and hydrobromic acid according to a fixed molar ratio. Excess hydrobromic acid ensured complete dissolution of $Pb(Ac)_2{\cdot}3H_2O$. $Pb(Ac)_2{\cdot}3H_2O$ was dissolved in the HBr solution and stirred at 80 °C to obtain a clear solution, and then methylamine aqueous solution and formamidine acetate were added. After stirring and heating for 1–2 hours, an $MA_{0.89}FA_{0.11}PbBr_3$ orange-red precipitate formed at the bottom. The powder was collected by filtration using a Buchner funnel, washed several times with anhydrous ethanol, and dried at 80 °C for 24 hours to obtain the final $MA_{0.89}FA_{0.11}PbBr_3$ powder.

2.3 Synthesis of $MA_{0.89}FA_{0.11}PbBr_3$ and $MA_{0.89}FA_{0.11}PbBr_3$:Tb single crystals

The $MA_{0.89}FA_{0.11}PbBr_3$ powder was dissolved in DMF solution and stirred overnight at room temperature. The precursor solution was filtered using a 0.45 μm pore size PTFE filter. For $MA_{0.89}FA_{0.11}PbBr_3$:Tb single crystal growth, a specific ratio of rare-earth acetate hydrate and a trace amount of hydrobromic acid were added to the $MA_{0.89}FA_{0.11}PbBr_3$ precursor solution. To control nucleation and suppress secondary nucleation, poly(ethylene glycol) was added as a polymer additive, consistent with the method described in the main text. The precursor solution was placed on a hot stage at 55–75 °C for 6–12 hours to grow $MA_{0.89}FA_{0.11}PbBr_3$ single crystals.

2.4 Characterization

The crystal structure was characterized using an X-ray powder diffractometer (D8 Advance, Bruker) with Cu Kα1 radiation (λ = 1.5406 Å). UV-Vis absorption spectra of the crystals were collected using a U-3900H (Hitachi) spectrometer equipped with an integrating sphere. Steady-state and time-resolved photoluminescence (TRPL) spectra were measured using an FLS-1000 fluorescence spectrometer (Edinburgh Instruments) at a 375 nm excitation wavelength. Elemental content in the crystals was measured using an ICP-AES (Ptima8300). X-ray fluorescence (XRF) mapping and line-scan analyses were performed using a micro-XRF spectrometer (Bruker M4 Tornado PLUS) to evaluate the spatial distribution of Tb^{3+} within the crystal lattice. X-ray photoelectron spectroscopy (XPS) measurements were performed on a Thermo Fisher ESCALAB 250Xi system. Electrical contacts were made by thermally evaporating 100 nm thick gold electrodes onto the crystal surfaces using a VZZ-300A high-vacuum thermal evaporator. Dark current–voltage characteristics were measured using a Keithley 2400 source meter to determine carrier mobility and trap density. The gamma-ray detector measurement platform utilized a charge-sensitive preamplifier (Shaanxi Dicreate, MA-01A), known for its low noise and high gain charge sensitivity.

3. Results and discussion

The synthesized large, high-quality RE-doped HP single crystals faces multiple challenges: doping-induced lattice strain, secondary nucleation, by-product formation, and the poor solubility of rare-earth reagents in organic solvents. By systematically optimizing crystallization parameters (precursor stoichiometry, growth temperature, and solution concentration) and employing a polymer additive to control nucleation,[21] we suppressed parasitic nucleation and synthesized a series of large $MA_{0.89}FA_{0.11}PbBr_3$:Tb single crystals (10–16 mm) with Tb/Pb ratios between 0.13% and 0.67% (Fig. 1a). Powder XRD patterns and Rietveld refinements proved the lattice incorporation of Tb^{3+} (Table S1). The notations 0.5Tb, 1Tb, 2Tb, and 5Tb denote the nominal Tb/Pb molar percentage in the precursor feed. They are adopted hereafter for conciseness. Crystals with nominal Tb/Pb ratios from 0.5% to 5% were synthesized, with the actual Tb incorporation (0.13% to 0.67%) as measured by ICP-AES. Increasing the Tb/Pb ratio systematically shifted all diffraction peaks to higher angles, indicating a progressive unit cell contraction while maintaining the cubic $Pm\bar{3}m$ phase.[21] For instance, the (211) peak shifted from 37.089° in the $MA_{0.89}FA_{0.11}PbBr_3$ crystal to 37.305° in its doped counterpart, corresponding to a reduction in the lattice constant from 5.9309 Å to 5.8988 Å (Fig. 1c and d). This lattice contraction might have originated from substituting the larger Pb^{2+} ions (119 pm) with smaller Tb^{3+} ions (92.3 pm), as illustrated in Fig. 1b. The monotonic change in lattice parameter with the Tb-doping concentration, along with the lack of secondary phases in XRD, demonstrates the successful and homogeneous

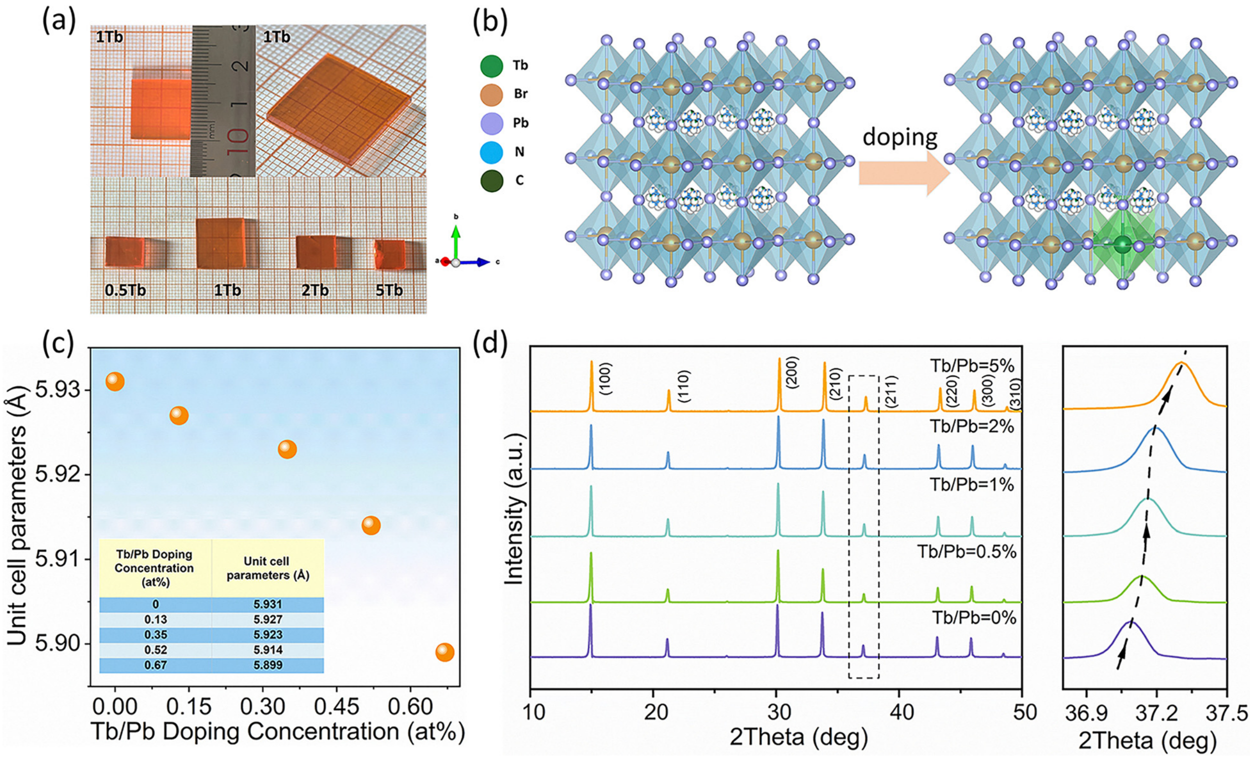

Tb/Pb Doping Concentration (at%)	Unit cell parameters (Å)
0	5.931
0.13	5.927
0.35	5.923
0.52	5.914
0.67	5.899

Fig. 1 Crystal structure and composition of $MA_{0.89}FA_{0.11}PbBr_3$:Tb single crystals. (a) Photographs of crystals with increasing Tb/Pb ratios. (b) Schematic of the crystal structure before and after Tb^{3+} doping. (c) Lattice parameter *versus* Tb/Pb ratio. (d) XRD patterns with a magnified view of the peak shift.

integration of Tb^{3+} into the perovskite lattice, in line with prior studies on RE-doped systems.[22,23]

The presence of terbium in the perovskite crystals and its trivalent oxidation state were observed by X-ray photoelectron spectroscopy (XPS), combined with X-ray fluorescence (XRF) mapping and inductively coupled plasma atomic emission spectroscopy (ICP-AES) for elemental quantification. Survey scans of the $MA_{0.89}FA_{0.11}PbBr_3$ crystal showed characteristic Pb 4f, N 1s, C 1s, and Br 3d peaks of terbium in the trivalent state.[24,25] Quantitative ICP-AES analysis proved a correlation between the actual Tb/Pb ratio in the crystals and the nominal feed ratio, demonstrating high doping efficiency (Fig. 2c and Table S2). The XPS and ICP-AES show that Tb^{3+} ions are incorporated into the crystal lattice.

To investigate whether rare-earth doping in single crystals is uniform or non-uniform, we employed X-ray fluorescence (XRF) mapping (Fig. S3–S7). Fig. S3 presents the mapping of Pb, Br, and Tb on the bottom surface of the 1% Tb-doped crystal, with a scanning area of 5 mm × 5 mm. The results indicate that all three elements are uniformly distributed. Subsequently, line scans were performed on the four samples to examine the distribution of Tb concentration. The results show that Tb characteristic peaks (Lα position 6.2 keV) were observed in all samples, with higher doping concentrations corresponding to higher peak counts. For the 0.5% and 1% Tb-doped crystals, the Tb concentration remained nearly constant, indicating uniform doping distribution. However, as the doping concentration increased, the Tb count rate exhibited fluctuations, albeit within a limited range. This observation suggests that higher doping concentrations may induce inhomogeneity in rare-earth element distribution.

The Tb-doping significantly modulates the optical properties of $MA_{0.89}FA_{0.11}PbBr_3$ single crystals. UV-Vis absorption spectra of $MA_{0.89}FA_{0.11}PbBr_3$:Tb show a systematic red-shift of the absorption edge with increasing nominal Tb/Pb feed ratio (Fig. 3a). Tauc plot analysis indicates a decreased bandgap from 2.183 eV ($MA_{0.89}FA_{0.11}PbBr_3$) to 2.138 eV (Tb/Pb = 5%) (Table S3). This bandgap modulation maybe attributed to the lattice contraction induced by the substitution of smaller Tb^{3+} ions for Pb^{2+} ions, consistent with the XRD analysis. X-ray photoelectron spectroscopy (XPS) confirms the trivalent state of terbium in the doped crystals. The high-resolution Tb 3d spectrum exhibits distinct peaks at 1243 eV and 1277 eV, corresponding to the Tb $3d_{5/2}$ and Tb $3d_{3/2}$ core levels, respectively (Fig. 2b).

These binding energies are characteristic of Tb^{3+}, proving the presence of bandgap narrowing from 2.183 eV ($MA_{0.89}FA_{0.11}PbBr_3$) to 2.138 eV by substituting smaller Tb^{3+} for Pb^{2+}, consistent with our XRD analysis (Table S3). Steady-state photoluminescence (PL) spectra, acquired under identical conditions, demonstrate a nearly 20-fold enhancement in emission intensity at 575 nm for the optimally doped (Tb/Pb = 1%) crystal compared to its $MA_{0.89}FA_{0.11}PbBr_3$ counterpart (Fig. 3b). Time-resolved photoluminescence (TRPL) decay curves, fitted with a biexponential function, show a dramatic increase in the bulk carrier lifetime (τ), rising from 197 ns in the undoped

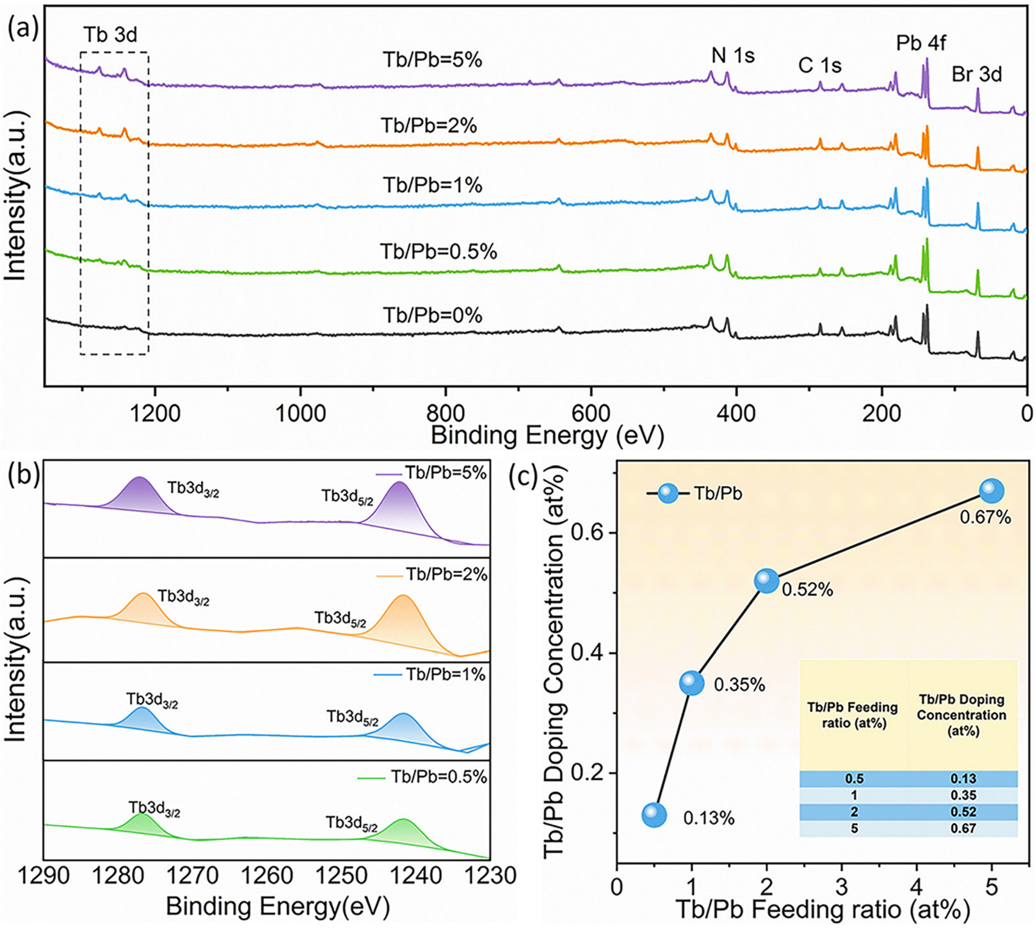

Fig. 2 Compositional analysis of $MA_{0.89}FA_{0.11}PbBr_3$:Tb: (a) XPS survey scans, (b) high-resolution Tb 3d spectra showing the Tb^{3+} state, and (c) doping efficiency determined by ICP-AES.

crystal to a maximum of 4422 ns at 1% Tb doping—an improvement of over 22-fold (Fig. 3c, d and Fig. S1). This trend of extended carrier lifetime aligns with the known role of rare-earth elements in suppressing non-radiative traps.[26] The observed bandgap widening, enhanced PL intensity, and greatly extended carrier lifetime together suggest that Tb^{3+} incorporation may passivate non-radiative recombination centers within the crystal lattice.

The space-charge-limited current (SCLC) technology is introduced to illustrate the enhancement of charge transport properties due to the Tb-doping. Shown in Fig. S8 is a schematic of the photodetector device constructed from $MA_{0.89}FA_{0.11}PbBr_3$:Tb single crystals, featuring a vertical architecture in which the perovskite crystal is sandwiched between a pair of gold (Au) electrodes. To evaluate the electrical characteristics of the device, current–voltage (I–V) measurements were carried out using a semiconductor parameter analyzer. Space-charge-limited current (SCLC) measurements were further employed to quantify the trap density (n_t) and carrier mobility (μ) of the single crystals. The resulting I–V curves display three characteristic regimes: an ohmic region (n = 1), a trap-filled region (n > 3), and a Child's law region (n = 2). Based on the trap-filled limit voltage (V_{TFL}), the defect density n_t was derived using the Mott–Gurney equation:

$$n_t = \frac{2V_{TFL}\varepsilon\varepsilon_0}{eL^2}$$

where L is the crystal thickness, ε is the relative permittivity, ε_0 is the vacuum permittivity, and e is the elementary charge. The carrier mobility μ is extracted from the Child's law region (third region), where current follows a quadratic dependence on voltage, using the Mott–Gurney equation:

$$\frac{8J_D L^3}{9\varepsilon\varepsilon_0 V^2}$$

where J_D is the current density and V is the applied voltage. Based on this analysis, the I–V curves of the single crystals exhibit three distinct regimes: an ohmic region (first region, n = 1), a trap-filled limited region (second region, n > 3), and a Child's law region (third region, n = 2.). By fitting the third region, the carrier mobilities of $MA_{0.89}FA_{0.11}PbBr_3$ and $MA_{0.89}FA_{0.11}PbBr_3$:Tb single crystals were calculated. Comparative I–V curves for the $MA_{0.89}FA_{0.11}PbBr_3$ and optimally doped (Tb/Pb = 1%) show a near-tripling of carrier mobility from 55.4 $cm^2\ V^{-1}\ s^{-1}$ to

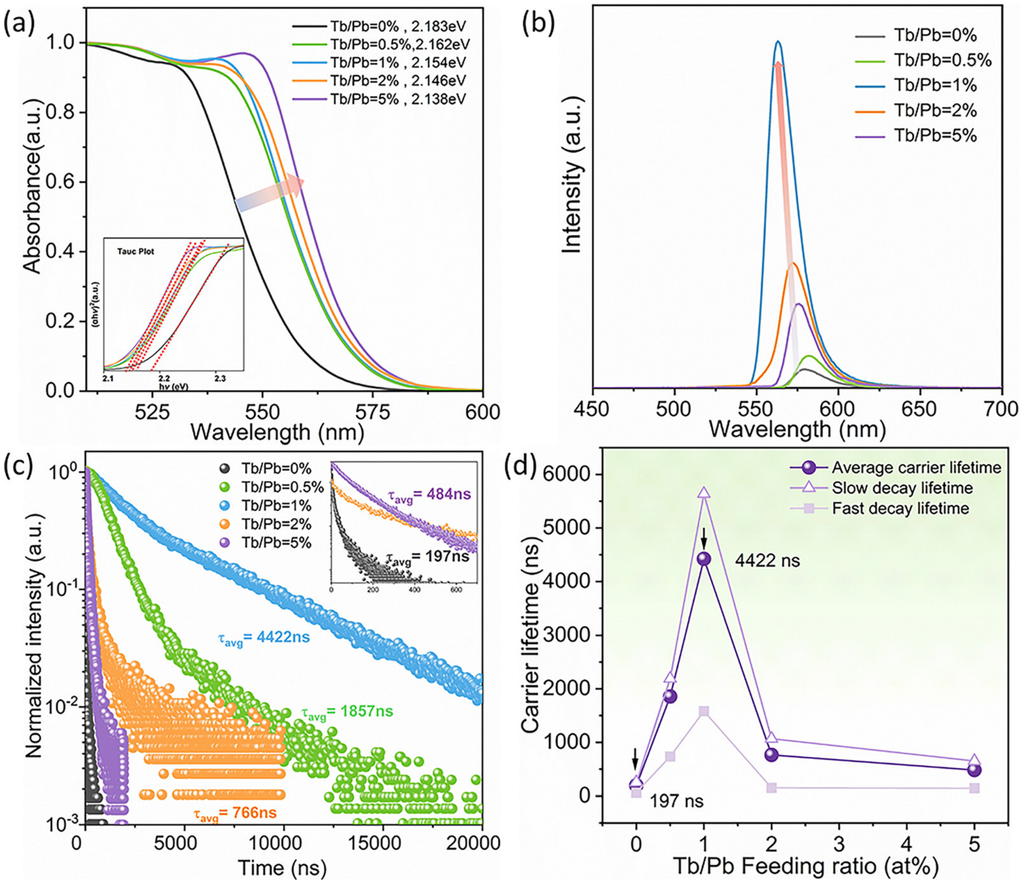

Fig. 3 Effects of Tb doping on optoelectronic properties: (a) UV-Vis spectra and bandgap narrowing, (b) steady-state PL intensity, (c) time-resolved PL decays, and (d) carrier lifetime *versus* doping concentration.

153.6 $cm^2\ V^{-1}\ s^{-1}$ in the $MA_{0.89}FA_{0.11}PbBr_3$ sample, alongside an order-of-magnitude reduction in trap density from 1.04×10^{10} cm^{-3} to 1.86×10^9 cm^{-3} (Fig. 4c, d and Fig. S9). This simultaneous suppression of trap density and boost in mobility agree with reports on other RE-doped perovskites[20] and align with our TRPL results (Table S4). The drastic reduction in charge trapping sites diminishes carrier scattering, thereby enhancing mobility, while also curbing nonradiative recombination pathways to extend the carrier lifetime (Fig. 3d).

The optimized charge transport properties of the Tb-doped crystals yield exceptional gamma-ray detection performance. Detectors with an Au/perovskite/Bi architecture (Fig. 5a and Fig. S10) were evaluated under a 10 V bias using a ^{241}Am15.7% (Fig. 5c). In contrast, the detector based on the optimally doped $MA_{0.89}FA_{0.11}PbBr_3$:1Tb crystal exhibited a well-defined photopeak with a dramatically improved ER of 4.3% (Fig. 5d). This substantial peak narrowing from minimized charge trapping losses can be attributed to the order-of-magnitude lower trap density and significantly higher carrier mobility. The energy resolution depended strongly on the Tb/Pb ratio, with optimal performance at the 1% nominal doping level (Fig. 5b), consistent with the peak carrier lifetime and mobility (Fig. S11). As shown in Fig. 5e, the $MA_{0.89}FA_{0.11}PbBr_3$:Tb gamma-detector achieves a better energy resolution performance compared with literature reports.[12–14,26–29] This result unambiguously validates Tb doping as a highly effective strategy for developing high-performance radiation sensing materials.

4. Conclusions

In this work, we demonstrate that rare-earth doping of HP single crystals, achieved through nucleation control and precursor regulation, can reach concentrations of up to 0.67%. The XRF mapping further corroborates the uniform distribution of Tb^{3+} within the crystal at a low Tb/Pb ratio ($\leq$0.35%), which is expected to contribute to the structural and electronic homogeneity crucial for reproducible detector performance. The incorporation of rare-earth ions induces lattice contraction and decreases the bandgap. More importantly, it significantly enhances semiconductor charge transport properties, including increased carrier mobility and the prolonged carrier lifetime—by up to a factor of 22 in average carrier lifetime (from 196 ns to 4422 ns). The improvement in semiconductor performance led to a substantial enhancement in gamma-ray detector performance, with the energy resolution improving from 15.7% to 4.3%.

While the optimization of HP single crystals has traditionally relied on compositional engineering or growth method

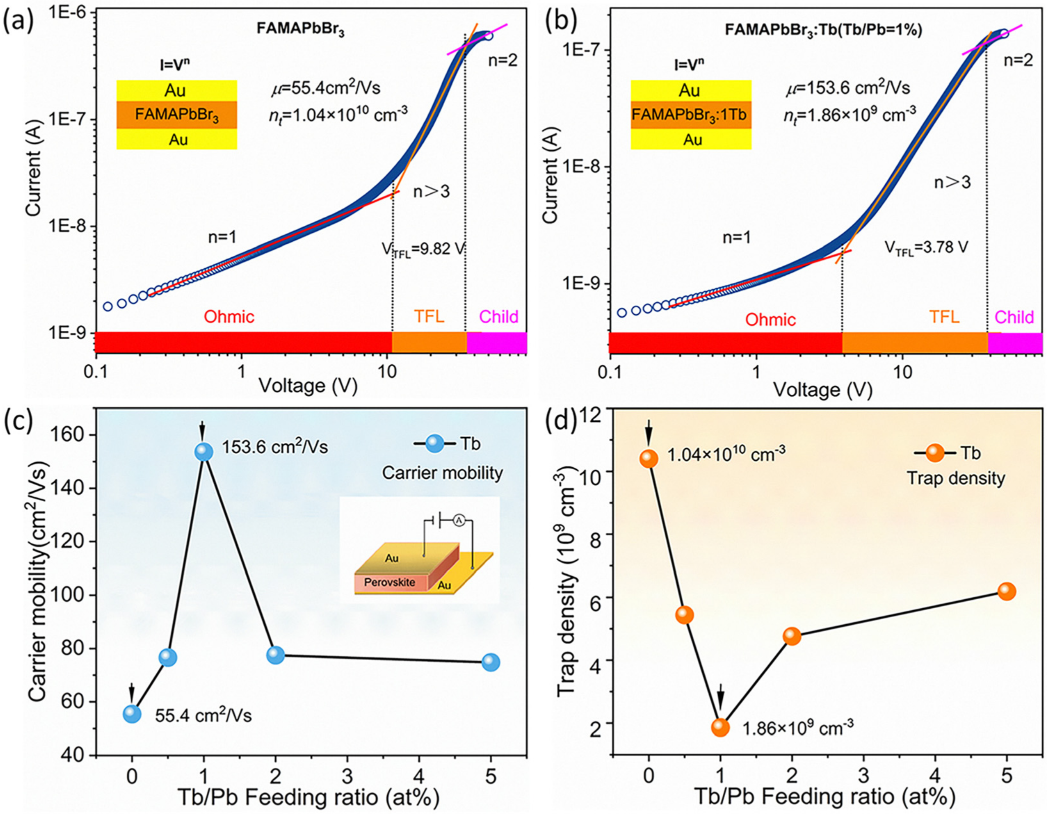

Fig. 4 Electrical characterization of $MA_{0.89}FA_{0.11}PbBr_3$ single crystals with varying Tb doping levels: (a) current–voltage (*I*–*V*) curves of the photodetector based on $MA_{0.89}FA_{0.11}PbBr_3$, (b) *I*–*V* curves of the photodetector with 1Tb doping, (c) carrier mobility as a function of Tb concentration, and (d) trap density as a function of Tb concentration.

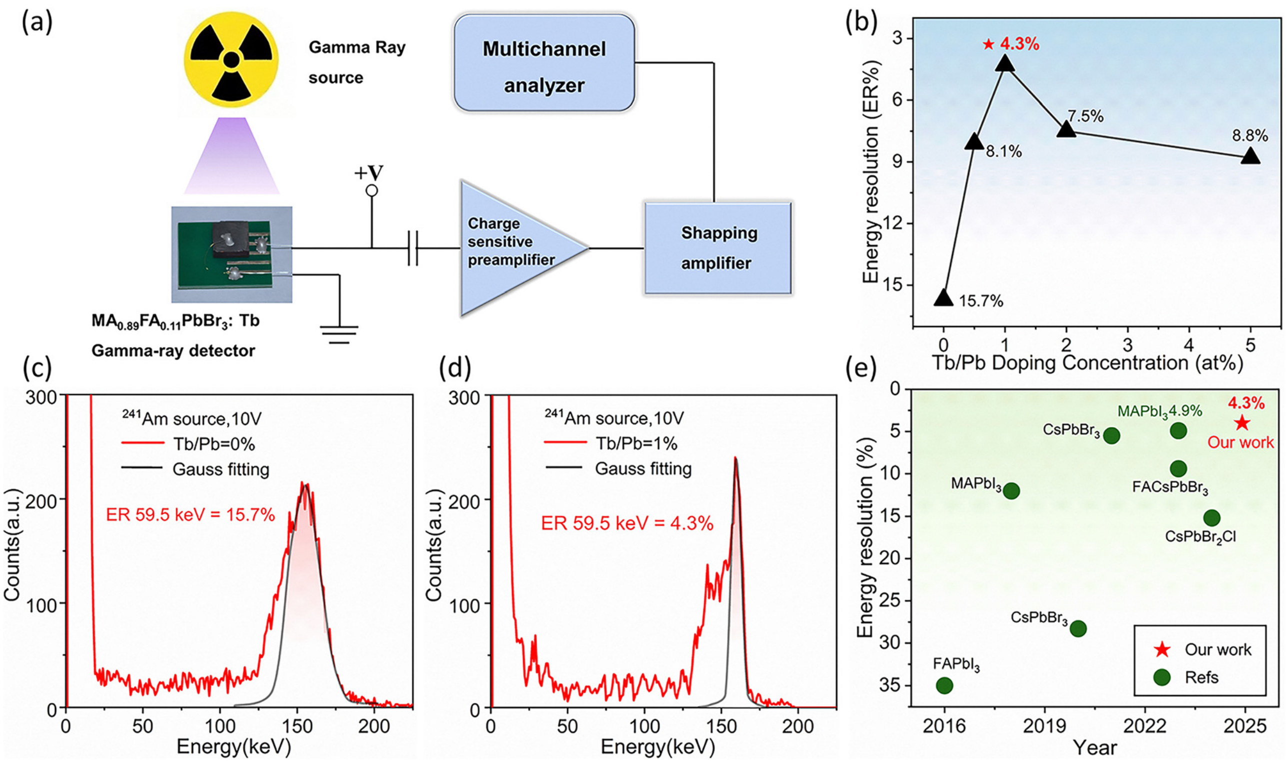

Fig. 5 High-performance gamma-ray detection: (a) measurement setup, (b) energy resolution *vs.* Tb/Pb ratio, (c) and (d) pulse-height spectra of the $MA_{0.89}FA_{0.11}PbBr_3$ (15.7% ER) and 1% Tb-doped (4.3% ER) detectors for 59.5 keV γ-rays, and (e) performance comparison with reported perovskite detectors.[12–14,27–30]

refinement, this work establishes rare-earth doping as an effective alternative pathway. Specifically, an optimal Tb/Pb ratio of 0.35% was identified in the $MA_{0.89}FA_{0.11}PbBr_3$:Tb system. Nevertheless, studies on rare-earth doping for improving HPs' semiconductor properties remain limited. Dark current–voltage measurements indicate a reduction in trap density, yet the underlying mechanisms require further investigation. We conclude that rare-earth doping represents a viable and promising route for advancing perovskite-based radiation detectors, with meaningful implications for future industrial development.

Author contributions

Qian Zhang carried out the crystal growth, characterization, device fabrication and testing and wrote the initial draft. Lin Ma designed the experiments, supervised the data analysis, and revised the manuscript. Guowei Wang assisted in manuscript revision. Yuhang Huang and Luyang Du synthesized the raw materials. Taifeng Lin provided guidance on spectroscopic measurements. Zhengguang Yan supervised the data analysis and manuscript revision. All authors reviewed and approved the final manuscript.

Conflicts of interest

There are no conflicts to declare.

Data availability

All data supporting the findings of this study are available within the main article and its accompanying supplementary information (SI). Supplementary information is available. See DOI: **https://doi.org/10.1039/d6qm00058d**.

Acknowledgements

The authors acknowledge the Fundamental Research Funds of this project: the National Science Fund for Distinguished Young Scholars (no. 12304004), the Excellent Research Group Program (52588202), the National Key R&D Program of China (2024YFA1408000), and the National Natural Science Foundation of China (general program no. 101020012021).

Notes and references

1 C. Zuo, H. J. Bolink, H. Han, J. Huang, D. Cahen and L. Ding, Advances in perovskite solar cells, *Adv. Sci.*, 2016, **3**, 1500324.
2 J. Guo, B. Wang, D. Lu, T. Wang, T. Liu, R. Wang, X. Dong, T. Zhou, N. Zheng and Q. Fu, Ultralong carrier lifetime exceeding 20 μs in lead halide perovskite film enable efficient solar cells, *Adv. Mater.*, 2023, **35**, 2212126.
3 X. Chu, Q. Ye, Z. Wang, C. Zhang, F. Ma, Z. Qu, Y. Zhao, Z. Yin, H.-X. Deng and X. Zhang, Surface in situ reconstruction of inorganic perovskite films enabling long carrier lifetimes and solar cells with 21% efficiency, *Nat. Energy*, 2023, **8**, 372–380.
4 B. Chen, S.-W. Baek, Y. Hou, E. Aydin, M. De Bastiani, B. Scheffel, A. Proppe, Z. Huang, M. Wei and Y.-K. Wang, Enhanced optical path and electron diffusion length enable high-efficiency perovskite tandems, *Nat. Commun.*, 2020, **11**, 1257.
5 X. Yang, Y. Fu, R. Su, Y. Zheng, Y. Zhang, W. Yang, M. Yu, P. Chen, Y. Wang and J. Wu, Superior carrier lifetimes exceeding 6 μs in polycrystalline halide perovskites, *Adv. Mater.*, 2020, **32**, 2002585.
6 Z. Lian, Q. Yan, T. Gao, J. Ding, Q. Lv, C. Ning, Q. Li and J.-L. Sun, Perovskite $CH_3NH_3PbI_3$(Cl) Single Crystals: Rapid Solution Growth, Unparalleled Crystalline Quality, and Low Trap Density toward 108 cm^{-3}, *J. Am. Chem. Soc.*, 2016, **138**, 9409–9412.
7 C. Motta, F. El-Mellouhi and S. Sanvito, Charge carrier mobility in hybrid halide perovskites, *Sci. Rep.*, 2015, **5**, 12746.
8 Y. Wang, Y. Zhang, P. Zhang and W. Zhang, High intrinsic carrier mobility and photon absorption in the perovskite CH 3 NH 3 PbI 3, *Phys. Chem. Chem. Phys.*, 2015, **17**, 11516–11520.
9 A. Pasha, S. Akhil and R. G. Balakrishna, Reliability of 3D Cs 2 M+ M 3+ X 6 type absorbers for perovskite solar cells: assessing the figures of merit, *J. Mater. Chem. A*, 2021, **9**, 17701–17719.
10 J. Yang, W. Wang, C. Bao, W. Huang and J. Wang, Toward practical applications of perovskite photodetectors: Advantages and challenges, *Matter*, 2025, **8**, 102207.
11 Z. Ni, L. Zhao, Z. Shi, A. Singh, J. Wiktor, M. O. Liedke, A. Wagner, Y. Dong, M. C. Beard and D. J. Keeble, Identification and suppression of point defects in bromide perovskite single crystals enabling gamma-ray spectroscopy, *Adv. Mater.*, 2024, **36**, 2406193.
12 Y. He, M. Petryk, Z. Liu, D. G. Chica, I. Hadar, C. Leak, W. Ke, I. Spanopoulos, W. Lin and D. Y. Chung, CsPbBr3 perovskite detectors with 1.4% energy resolution for high-energy γ-rays, *Nat. Photonics*, 2021, **15**, 36–42.
13 L. Zhao, Y. Zhou, Z. Shi, Z. Ni, M. Wang, Y. Liu and J. Huang, High-yield growth of FACsPbBr3 single crystals with low defect density from mixed solvents for gamma-ray spectroscopy, *Nat. Photonics*, 2023, **17**, 315–323.
14 Y. Song, L. Wang, Y. Shi, W. Bi, J. Chen, M. Hao, A. Wang, X. Yang, Y. Sun and F. Yu, Detector-grade perovskite single-crystal wafers via stress-free gel-confined solution growth targeting high-resolution ionizing radiation detection, *Light: Sci. Appl.*, 2023, **12**, 85.
15 H. Dong, C. Ran, W. Gao, M. Li, Y. Xia and W. Huang, Metal Halide Perovskite for next-generation optoelectronics: progresses and prospects, *eLight*, 2023, **3**(1), 3.
16 G. Pan, X. Bai, D. Yang, X. Chen, P. Jing, S. Qu, L. Zhang, D. Zhou, J. Zhu and W. Xu, Doping lanthanide into perovskite nanocrystals: highly improved and expanded optical properties, *Nano Lett.*, 2017, **17**, 8005–8011.

17 L. Zheng, K. Wang, T. Zhu, L. Liu, J. Zheng and X. Gong, Solution-processed ultrahigh detectivity photodetectors by hybrid perovskite incorporated with heterovalent neodymium cations, *ACS Omega*, 2019, **4**, 15873–15878.

18 Y. Zhang, L. Xu, J. Sun, Y. Wu, Z. Kan, H. Zhang, L. Yang, B. Liu, B. Dong and X. Bai, 24.11% High Performance Perovskite Solar Cells by Dual Interfacial Carrier Mobility Enhancement and Charge-Carrier Transport Balance, *Adv. Energy Mater.*, 2022, **12**, 2201269.

19 S. Rong, Y. Xiao, J. Jiang, Q. Zeng and Y. Li, Strongly Enhanced Photoluminescence and Photoconductivity in Erbium-Doped MAPbBr3 Single Crystals, *J. Phys. Chem. C*, 2020, **124**, 8992–8998.

20 L. Zi, W. Xu, R. Sun, Z. Li, J. Zhang, L. Liu, N. Wang, Y. Wang, N. Ding and J. Hu, Lanthanide-doped MAPbI3 single crystals: fabrication, optical and electrical properties, and multi-mode photodetection, *Chem. Mater.*, 2022, **34**, 7412–7423.

21 L. Ma, Z. Yan, X. Zhou, Y. Pi, Y. Du, J. Huang, K. Wang, K. Wu, C. Zhuang and X. Han, A polymer controlled nucleation route towards the generalized growth of organic-inorganic perovskite single crystals, *Nat. Commun.*, 2021, **12**, 2023.

22 Q. Hu, Z. Li, Z. Tan, H. Song, C. Ge, G. Niu, J. Han and J. Tang, Rare earth ion-doped CsPbBr3 nanocrystals, *Adv. Opt. Mater.*, 2018, **6**, 1700864.

23 W. Duan, L. Hu, W. Zhao and X. Zhang, Rare-earth ion-doped perovskite quantum dots: synthesis and optoelectronic properties, *J. Mater. Sci.: Mater. Electron.*, 2022, **33**, 19019–19025.

24 S. S. Mali, J. V. Patil, S. R. Rondiya, N. Y. Dzade, J. A. Steele, M. K. Nazeeruddin, P. S. Patil and C. K. Hong, Terbium-Doped and Dual-Passivated γ-CsPb(I1−xBrx)3 Inorganic Perovskite Solar Cells with Improved Air Thermal Stability and High Efficiency, *Adv. Mater.*, 2022, **34**(29), 2203204.

25 X. Duan, K. Nie, Z. Hu, X. Zhang, R. Zhou, W. Dai, L. Mei, L. Wang, H. Wang and X. Ma, Enhancement of orange emission in terbium-doped lead-free halide perovskite for flexible functional fibers and light-emitting diodes, *Chem. Eng. J.*, 2024, **480**(15), 147957.

26 Z. Song, W. Xu, Y. Wu, S. Liu, W. Bi, X. Chen and H. Song, Incorporating of lanthanides ions into perovskite film for efficient and stable perovskite solar cells, *Small*, 2020, **16**, 2001770.

27 L. Zhao, Y. Zhou, Z. Shi, Z. Ni, M. Wang, Y. Liu and J. Huang, High-yield growth of FACsPbBr3 single crystals with low defect density from mixed solvents for gamma-ray spectroscopy, *Nat. Photonics*, 2023, **17**, 315–323.

28 S. Yakunin, D. N. Dirin, Y. Shynkarenko, V. Morad, I. Cherniukh, O. Nazarenko, D. Kreil, T. Nauser and M. V. Kovalenko, Detection of gamma photons using solution-grown single crystals of hybrid lead halide perovskites, *Nat. Photonics*, 2016, **10**, 585–589.

29 L. Pan, Y. Feng, P. Kandlakunta, J. Huang and L. R. Cao, Performance of perovskite CsPbBr 3 single crystal detector for gamma-ray detection, *IEEE Trans. Nucl. Sci.*, 2020, **67**, 443–449.

30 Y. He, W. Ke, G. C. Alexander, K. M. McCall, D. G. Chica, Z. Liu, I. Hadar, C. C. Stoumpos, B. W. Wessels and M. G. Kanatzidis, Resolving the energy of γ-ray photons with MAPbI3 single crystals, *ACS Photonics*, 2018, **5**, 4132–4138.